

Spectroscopic detection of Altair's non-radial pulsations^{*}

Michel Rieutord¹, Pascal Petit¹, Daniel Reese², Torsten Böhm¹, Arturo López Ariste¹,
Giovanni M. Mirouh³, and Armando Domiciano de Souza⁴

¹ IRAP, Université de Toulouse, CNRS, UPS, CNES, 14, avenue Édouard Belin, F-31400 Toulouse, France

² LESIA, Observatoire de Paris, Université PSL, CNRS, Sorbonne Université, Univ. Paris Diderot, Sorbonne Paris Cité, 5 place Jules Janssen, 92195 Meudon, France

³ Departamento de Física Teórica y del Cosmos, Universidad de Granada, Campus de Fuentenueva s/n, E-18071 Granada, Spain

⁴ Université Côte d'Azur, Observatoire de la Côte d'Azur, CNRS, Laboratoire Lagrange, Bd de l'Observatoire, CS 34229, 06304 Nice cedex 4, France

e-mail: [Michel.Rieutord,Pascal.Petit,tboehm,Arturo.Lopezariste]@irap.omp.eu,daniel.reese@obspm.fr,
gmm@ugr.es,armando.domiciano@oca.eu

September 21, 2022

ABSTRACT

Context. Rapid rotation is a common feature of early-type stars but which remains a challenge for the models. The understanding of its effect on stellar evolution is however imperative to interpret the observed properties of numerous stars.

Aims. We wish to bring more observational constraints on the properties of fast rotating stars, especially on their oscillation modes.

Methods. We focus on the nearby star Altair which is known as a very rapidly rotating star with an equatorial velocity estimated recently at 313 km/s. We observed this star with the high-resolution spectropolarimeter Neo-Narval during six nights, with one night of interruption, in September 2020.

Results. We detect significant line profile variations on the mean line profile of the spectra. Their time-frequency analysis shows that these variations are induced by gravito-inertial waves propagating at Altair's surface with azimuthal wavenumbers of order $m = 10 - 15$. With a preliminary computation of the eigenspectrum using the most recent concordance model of Altair we can give a first modelling of the observed waves.

Conclusions. Altair was known as the brightest δ Scuti star. We now see that it is the brightest hybrid oscillating star with excited gravito-inertial waves and acoustic waves. Clearly, more observations and more advanced models are needed to explain the observations in greater details.

Key words. stars: rotation – stars: early-type

1. Introduction

At a distance of 5.13 pc, Altair (α Aql) is the closest early-type (A7V) fast rotating star to the Sun. As such, Altair has been intensively observed in interferometry (van Belle et al. 2001; Domiciano de Souza et al. 2005; Peterson et al. 2006; Monnier et al. 2007; Bouchaud et al. 2020; Spalding et al. 2022). An important result of interferometric observations is the determination of the inclination of Altair's rotation axis on the line-of-sight. The most recent value is $i = 50.7 \pm 1.2^\circ$ (Bouchaud et al. 2020). Since spectroscopy indicates that $v \sin i \simeq 227 \pm 11$ (Reiners & Royer 2004), 231 km/s (Takeda 2020), 242 km/s (Bouchaud et al. 2020), it turns out that Altair's equatorial velocity is likely over 300 km/s. This makes Altair rotating at 74% of its critical angular velocity. As a consequence it is strongly flattened by the centrifugal force, making its equatorial radius 22 % larger than the polar one. Hence, it is no surprise that such a star cannot be modelled with spherically symmetric mod-

els as is shown by its age undetermination. Indeed, using 1D-models Suárez et al. (2005) indicate a range of 225-775 Myrs, while Domiciano de Souza et al. (2005) mention another range in between 1.2 and 1.4 Gyrs. Thus, Altair turns out to be the star to be used for testing 2D models like ESTER models (Espinosa Lara & Rieutord 2013; Rieutord et al. 2016). This test was the main objective of Bouchaud et al. (2020) who devised the first concordance model of Altair. Bouchaud et al. (2020) indeed managed to match the interferometric, spectroscopic and asteroseismic observations with a single 2D-model. This model indicates that Altair is 100 Myrs old thus barely off the ZAMS as suspected by Peterson et al. (2006). In this 2D-modelling, Bouchaud et al. (2020) showed that asteroseismology was key to lift some degeneracy on the mass of Altair. Altair is indeed a δ Scuti star whose oscillations were first detected by Buzasi et al. (2005). Recently, Le Dizès et al. (2021) confirmed these δ Scuti oscillations and increased slightly the number of detected frequencies, thanks to the analysis of MOST (Microvariability and Oscillations of STars) satellite data (Walker et al. 2003). Le Dizès et al. (2021) also showed the variability of the modes amplitudes, and the

^{*} Based on observations obtained at the Télescope Bernard Lyot (TBL) at Observatoire du Pic du Midi, CNRS/INSU and Université de Toulouse, France.

probable coupling of the modes with thin convective layers not much below Altair’s surface.

In the present work we describe the first detection of non-radial pulsations of Altair with high resolution spectroscopy using the 2-meter Bernard Lyot telescope at the Pic-du-Midi. In the past similar detections have been made on very few rotating stars: e.g. γ Bootis with $v \sin i \simeq 127$ km/s (Ventura et al. 2007), or on spectroscopic binaries like RS Chamaeleontis (Böhm et al. 2009). However, Altair is the star with the largest $v \sin i$ where such oscillations are detected. Compared to photometric observations, spectroscopic ones give an indication of the mode azimuthal wavenumber which helps with mode identification and further constraining the fundamental parameters.

The paper is organised as follows: We first give a brief description of the data we use and their reduction (Sect. 2). This is followed by their analysis (Sect. 3) and a short discussion of the possible identification of modes (Sect. 4). We then revert to 2D models and discuss the comparison between data and model predictions (Sect. 5). Conclusions follow.

2. Observations and data reduction

Altair was observed during six nights in between 2 September and 8 September 2020 at the Pic-du-Midi with the spectropolarimeter Neo-Narval (see López Ariste et al. 2022, for a presentation of the instrument) at the Cassegrain focus of the Bernard Lyot Telescope. 643 spectra were obtained sampling the light of Altair every 3 min or so (see Tab. 1 for details). The duty cycle of these observations is however quite low at 0.21.

From the circular and linear spectropolarimetric data collected during this run, only the intensity signal was used. The data reduction was performed through the automated pipeline of the instrument, providing us with spectra covering the whole optical domain (380 to 1,050 nm) at a resolving power of around 65,000. The peak signal-to-noise ratio, defined per unit of spectral resolution, is typically close to 1,400. This latter value is reached at wavelengths close to 705 nm.

All observations were processed with the Least-Square Deconvolution method (Donati et al. 1997; Kochukhov et al. 2010) to extract a mean pseudo-line profile from every spectra. A list of around 6,300 photospheric lines deeper than 1% of the continuum was extracted from the VALD data base (Kupka et al. 1999), assuming a surface temperature equal to 7,500 K. According to Monnier et al. (2007), this temperature is representative of intermediate latitudes of this oblate star. The intensity signatures reported hereafter are qualitatively unchanged when adopting other line masks with temperatures chosen to match lower or higher latitudes. The LSD profile example shown in Fig. 1 (top) is dominated by rotational broadening. Once an averaged profile (of all observations collected during the same night) is subtracted, bumps and dips become visible within line profiles (Fig. 1 bottom).

3. Data analysis

Fig. 2 illustrates the way we see the Doppler shift of Altair according to the model of Bouchaud et al. (2020). This model also gives an equatorial rotation frequency of 3.08

| Night | JD _s -JD ₀ day | JD _e -JD ₀ day | $\langle \delta t \rangle$ seconds |
|----------------|---|---|---------------------------------------|
| 2-3 Sept. 2020 | 1.40711 | 1.59317 | 206 |
| 3-4 Sept. 2020 | 2.31025 | 2.57120 | 211 |
| 4-5 Sept. 2020 | 3.31218 | 3.56229 | 165 |
| 5-6 Sept. 2020 | 4.32412 | 4.57411 | 162 |
| 7-8 Sept. 2020 | 6.46547 | 6.55644 | 160 |
| 8-9 Sept. 2020 | 7.30241 | 7.56421 | 162 |

Table 1. Summary of the observations dates and the average period of time sampling $\langle \delta t \rangle$. JD_s and JD_e are the starting and ending Julian dates of the observations. The reference Julian date is JD₀=2459094.

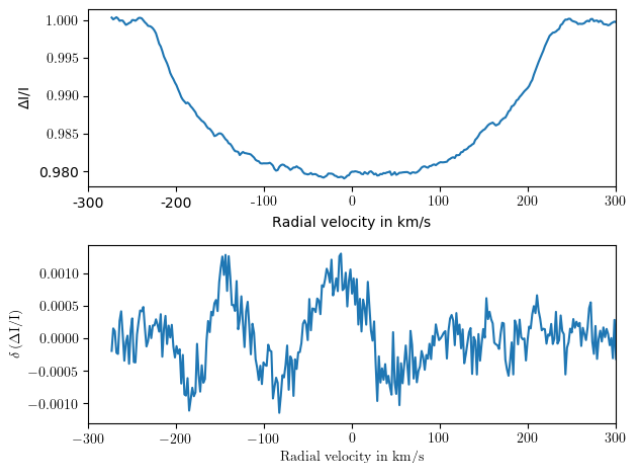


Fig. 1. Upper panel: example of an LSD profile of Altair’s spectrum. Bottom panel: the same LSD profile, after subtraction of the average of all available profiles of the same night.

c/d (Le Dizès et al. 2021), which we shall adopt when moving from the observer’s frame to the co-rotating frame. Any feature moving in the line profile may or may not move in longitude in the co-rotating frame.

Relative amplitudes of the detected features are typically of order 10^{-3} in intensity (Fig. 1 bottom) and look like wave trains propagating in the prograde direction as shown in Fig. 3’s left plots for all the nights. Typically, individual wave trains remain visible for roughly two hours.

We shall assume that these waves only propagate in longitude and that they are of the form $I(\theta) \exp(im\varphi - i\omega t)$, where (θ, φ) are the spherical angles of a point at Altair’s surface. If perturbations are concentrated around Altair’s equator we can easily relate the radial velocity V_r at which the perturbation occurs and the longitude by

$$\varphi_v = \arcsin \left(\frac{V_r}{V_{\text{eq}} \sin i} \right) \quad (1)$$

where V_{eq} is the equatorial velocity and i is the angle between the line of sight and the rotation axis. Of course V_r is corrected from the radial velocity of Altair. We shall call φ_v the virtual longitude to stress the fact that actually several longitudes contribute at a given radial velocity as is clear from the projected map shown in Fig. 2.

It is nevertheless interesting to see the azimuthal wavenumber m which is associated with the perturbations of the line if we replace the radial velocity coordinate by

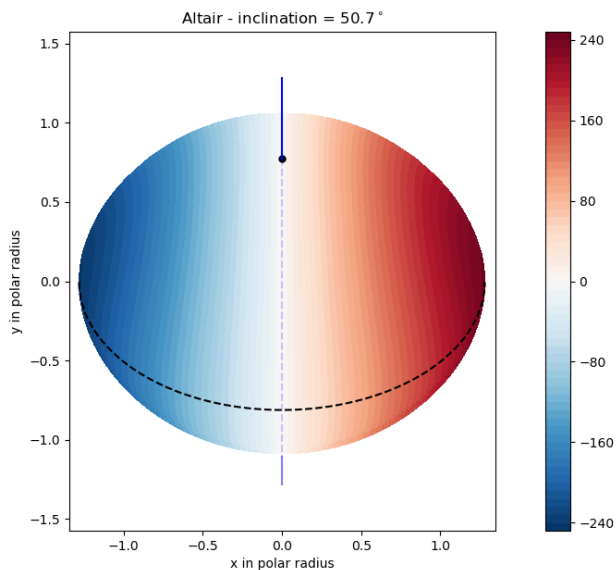


Fig. 2. The rotational velocity field of Altair projected along the line of sight according to the model of Bouchaud et al. (2020). Velocities are in km/s. The equator and North pole are marked out.

the virtual longitude. Hence, we get an information on the apparent m values contained in the signal (e.g. Böhm et al. 2009). To this end, we compute a Lomb-Scargle periodogram of the line profile fluctuations (like the one shown in Fig. 1 bottom) using the virtual longitude as the time analog¹. We choose the Lomb-Scargle periodogram instead of a simple Fourier transform since the data points are not regularly spaced in longitude (see below). This computation allows us to extract the azimuthal wavenumbers contained in the signal as a function of time as shown in Fig. 3 (right plots). These plots clearly show that wavenumbers around $m = 10$ are conspicuously detected. We also note that wavenumbers change with time. It may be a consequence of beating waves or some nonlinear evolution.

Beside the foregoing azimuthal analysis of the line profile fluctuations, we can also compute a Lomb-Scargle periodogram at a given virtual longitude. We thus calculate this periodogram selecting eight pixels around the line centre and thus exhibit for each night a few frequencies. The corresponding plots are still shown in Fig. 3 at the bottom for each night. There we clearly see that all detected frequencies lie in between ~ 20 and ~ 50 cycles/day (c/d).

The next step is to relate the frequencies and the azimuthal wavenumbers m . For that purpose we first fit each line profile fluctuation with a limited Fourier series, namely

$$\delta I(t, \varphi_v) = a(t) + \sum_{m=1}^{20} b_m(t) \cos(m\varphi_v) + c_m(t) \sin(m\varphi_v) \quad (2)$$

We then compute the Lomb-Scargle time periodogram of each coefficient $b_m(t)$ and $c_m(t)$, for all the chosen wavenumbers. We thus derive the transforms $\tilde{b}(m, \omega)$

¹ Lomb-Scargle periodogram are usually computed for time-dependent signals.

| | Frequency (c/d) | | $\langle A \rangle$ (ppm) | m |
|-------|--------------------|-------|------------------------------|-----|
| f_1 | 38.14 | 4.26 | 294±7 | 11 |
| f_2 | 43.63 | 3.59 | 210±6 | 13 |
| f_3 | 31.51 | 6.87 | 166±7 | 8 |
| f_4 | 25.32 | 6.84 | 123±6 | 6 |
| f_5 | 35.87 | 1.99 | 113±7 | 11 |
| f_6 | 31.13 | 6.49 | 102±6 | 8 |
| f_7 | 56.58 | 10.38 | 27±4 | 15 |

Table 2. List of oscillation frequencies that have been detected with their most probable azimuthal wavenumber (m). The first column of the frequencies are the one observed, while the second column gives the value in the corotating frame of Altair using a rotation frequency of 3.08 c/d (e.g. Le Dizès et al. 2021). $\langle A \rangle$ is the measured amplitude.

and $\tilde{c}(m, \omega)$, from which we compute the spectral power $P(m, \omega) = \sqrt{\tilde{b}^2 + \tilde{c}^2}$. As a result we obtain an $m - \omega$ diagram analogous to the famous $k - \omega$ diagram of solar eigenmodes (e.g. Gonzalez Hernandez et al. 1998; Gizon et al. 2010). This diagram, showing $P(m, \omega)$, is displayed for each night in Fig. 4.

As may be noted, spatial frequencies range from $m = 5$ to $m \simeq 18$ while time-frequencies stay in between 20 c/d and 50 c/d. The blue line on each diagram shows the frequency of a standing wave of azimuthal wavenumber m in the corotating frame, assuming a rotation period of 8 hrs deduced from the model of Altair by Bouchaud et al. (2020). We note that most of the modes are above that line showing that they are prograde modes in the corotating frame. Moreover, they are mostly in the inertial frequency band $-2f_{\text{rot}} \leq f_{\text{corot}} \leq 2f_{\text{rot}}$ or slightly above, thus indicating their nature, namely inertial or gravito-inertial modes (e.g. Rieutord & Valdettaro 1997; Dintrans et al. 1999; Dintrans & Rieutord 2000).

4. Mode detection and identification

The foregoing raw analysis showed that a set of waves are excited. To proceed towards their identification we first try to identify their azimuthal wavenumbers of their longitude dependence, namely their $\exp(im\varphi)$ -dependence. As illustrated in Fig. 5 (top) where we show the spectral perturbation generated by a purely sectoral mode, propagating over Bouchaud et al. (2020)'s model, with a latitude-longitude amplitude fluctuation like

$$\delta a \propto \sin^m \theta \exp(im\varphi), \quad (3)$$

with $m = 11$, the signal is neither periodic nor evenly sampled in longitude. Hence, the Fourier transform struggles to recover the right m . Fig. 5 shows that the Lomb-Scargle periodogram is more appropriate than the Fourier spectrum to recover the actual m of the signal.

To further progress, we compute the Lomb-Scargle periodogram of $b_m(t)$ and $c_m(t)$ combining all the nights' data. As expected from the $m - \omega$ diagram (Fig. 4), we detect the same frequency for several m 's, but with different amplitudes. Fig. 6 summarizes the results and shows the amplitude as a function of m for each given frequency. Obviously

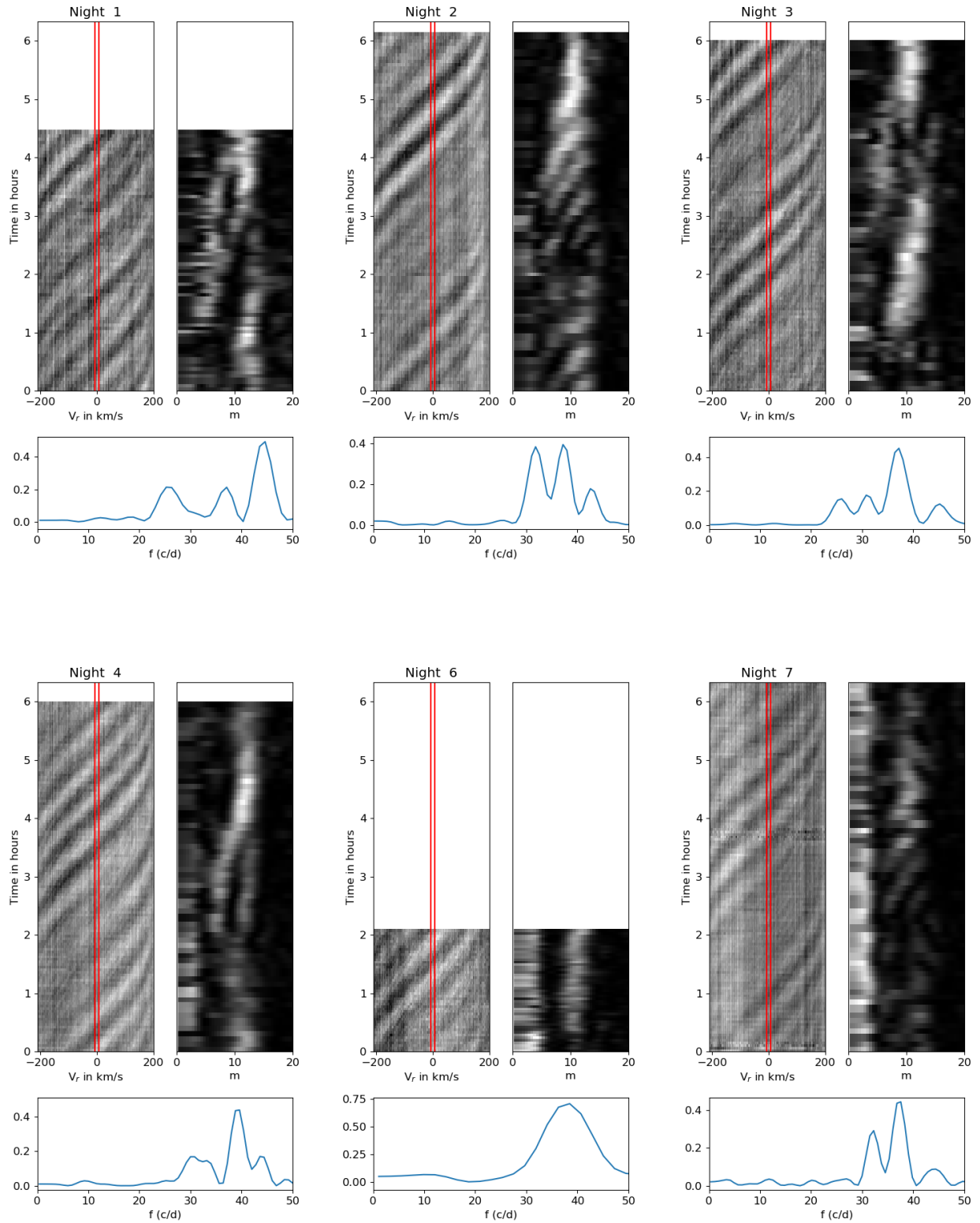


Fig. 3. Global view of the relative fluctuations in the mean line profile for each of the six nights of observation. For each night we show in the top left panel the signal as a function of time and radial velocity in km/s. In the top right panel we show the Lomb-Scargle periodogram of the line profile fluctuations in (virtual) longitude as a function of time and the azimuthal wavenumber m , while the bottom plot shows a Lomb-Scargle periodogram of the time variations of the intensity in the eight pixels at the line centre that are marked by the red lines in the top-left panels.

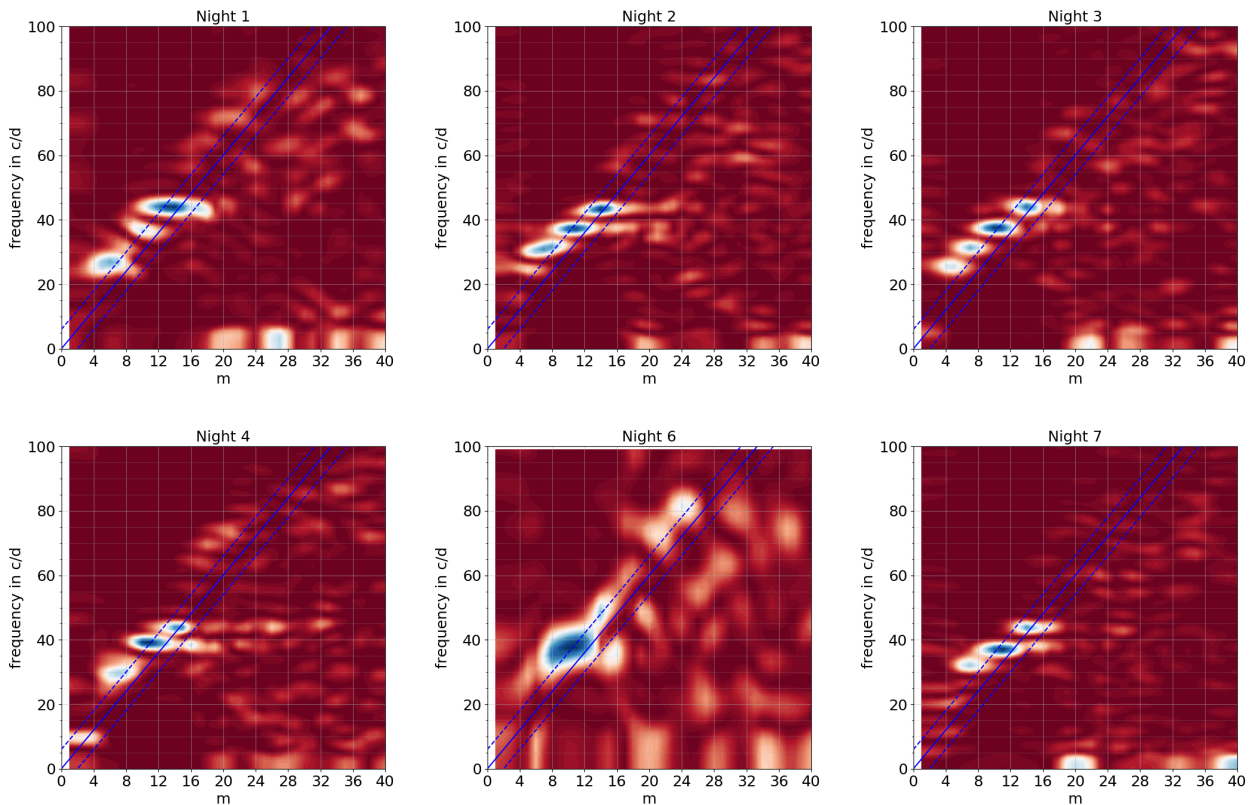


Fig. 4. $m - \omega$ diagram for the six nights showing the spectral power as a function of m and frequency in the observer's frame. The blue solid line shows the time frequency of a standing wave in the corotating frame characterized by wavenumber m . Modes above that line are prograde, and modes below that line are retrograde. The two dashed blue lines delineate the inertial frequency band.

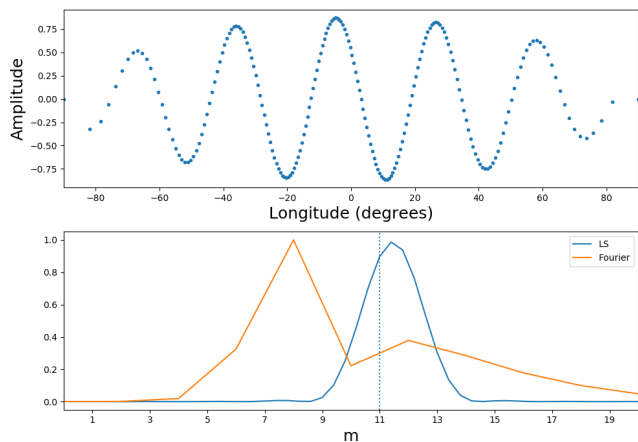


Fig. 5. Top: Simulation of the line profile perturbation induced by a purely sectoral mode with $m = 11$ (amplitude is arbitrary). Bottom: the Fourier spectrum of the signal and the Lomb-Scargle periodogram.

the most prominent wave oscillates at 38.14 c/d and seems to be associated with a $m = 11$ wavenumber. In Tab. 2, we list the frequencies that have been unambiguously detected. We also give the amplitude of the signal in ppm and the most probable azimuthal wavenumber m . As shown by Fig. 6, the association between frequency and wavenumber is not always clear.

Three of the detected frequencies (f_1, f_2, f_5) are clearly in the inertial frequency band, since they verify

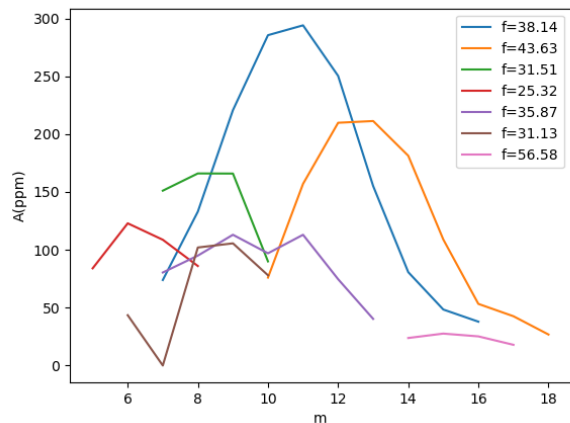


Fig. 6. Amplitude (in ppm) of the waves as a function of the azimuthal wavenumber used to do the projection of the Doppler signal. Waves are characterized by their frequency f given in c/d.

$f_{\text{corot}} \leq 2f_{\text{rot}}$, if we take $f_{\text{rot}} = 3.08$ c/d (see Sect. 3). The four other frequencies are also low frequencies only slightly above the inertial band. The modes associated with these frequencies are therefore gravito-inertial modes which may be either inertial modes (restored by Coriolis force) perturbed by a stable stratification or reciprocally, gravity modes perturbed by rotation (see Dintrens et al. 1999, for canonical examples).

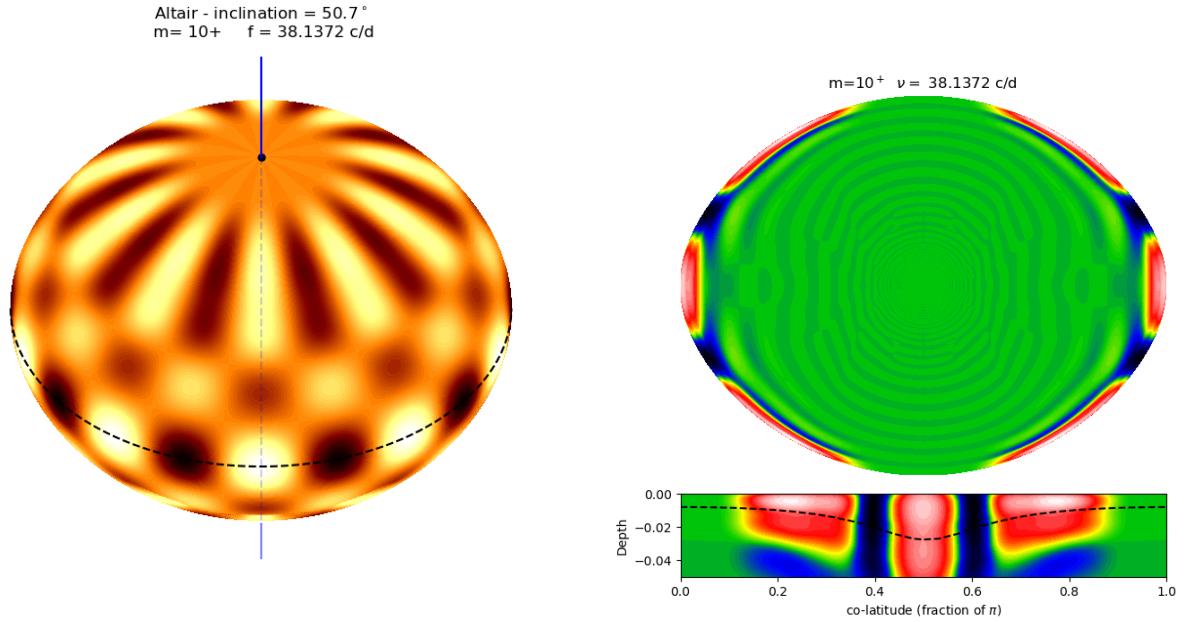


Fig. 7. Surface amplitude (left) and meridional cut of the kinetic energy density (right) of a gravito-inertial mode that may give a signal at $f=38.14$ c/d. The bottom plot at right is a zoom of the surface layers and the dashed line shows the $T=50,000$ K isotherm around which the second ionization of helium takes place. The depth is scaled by the polar radius of the model.

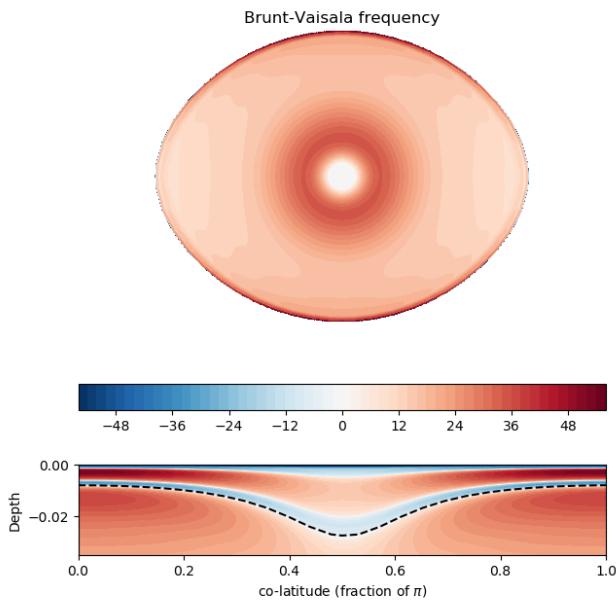


Fig. 8. Meridional section of the concordance model of Altair (e.g. Bouchaud et al. 2020) showing the Brunt-Väisälä frequency. Units on the color bar are in cycle/day. Negative values show the convectively unstable regions. The lower plot gives a zoomed-view of the surface layers and the dashed line shows the $T=50,000$ K isotherm around which the second ionization of helium takes place. Depth is scaled by the polar radius of the model.

| Parameters | ESTER model |
|-------------------------------------|-------------|
| M (M_{\odot}) | 1.863 |
| T_{pole} (K) | 8621 |
| T_{eq} (K) | 6780 |
| R_{pole} (R_{\odot}) | 1.568 |
| R_{eq} (R_{\odot}) | 2.011 |
| v_{eq} (km/s) | 313 |
| Ω_{eq} (Ω_k) | 0.744 |
| ε | 0.220 |
| Z | 0.0192 |
| X_{env} | 0.739 |
| X_{core} | 0.712 |

Table 3. Fundamental parameters of an ESTER model that matches the observational constraints on Altair derived by Bouchaud et al. (2020). $\varepsilon = 1 - R_{\text{pole}}/R_{\text{eq}}$ is the flattening, Z is metallicity and X the hydrogen mass fraction.

5. The word of models

5.1. Preliminary results

To have further insight into the waves that are seen in the present spectroscopic data, we now focus on the concordance model of Altair derived by Bouchaud et al. (2020), which we previously mentioned. We recall in Tab. 3 the fundamental parameters of this model that matches the constraints derived from interferometric, spectroscopic and seismic data. The latter data are frequencies obtained from WIRE photometry by Buzasi et al. (2005).

To further progress in the seismological properties of Altair, we computed some eigenmodes of the concordance model with the TOP code (Reese et al. 2021), which can

handle ESTER 2D models. We naturally focus on the observed frequencies but more precisely, we scanned the frequency band $f \pm 0.05$ c/d of each frequency listed in Tab. 2 for the three m 's around the most probable one. Hence, for the most prominent frequency, at 38.14 c/d, we investigate the frequency band [38.09, 38.19] c/d for azimuthal wavenumbers $m = 10, 11, 12$. We show in Fig. 7 a view of a mode which may give the signal observed at 38.14 c/d. Shifting this frequency in the co-rotating frame, namely

$$f_{\text{corot}} = f - m f_{\text{rot}}, \quad (4)$$

with $f_{\text{rot}} = 3.08$ c/d, we find that it either belongs to the inertial frequency band, if $m = 11$ or 12 , or is just above if $m = 10$. As shown in Fig. 7, the amplitude of such a mode is only significant near the surface. The meridional map of the Brunt-Väisälä frequency (Fig. 8) shows that such modes actually propagate over two convectively unstable layers sandwiching a stable one. The deeper unstable layer is associated with the second ionization of helium, which is the driver of the kappa-mechanism in δ Scuti stars (Baglin et al. 1973; Balona et al. 2015). The 50,000K isotherm, around which the second ionization of helium takes place, is depicted as a dashed line in Fig. 7 (bottom right) and Fig. 8 (bottom), showing that this mode may possibly be destabilized by the kappa mechanism.

The foregoing mode may be used to constrain the differential rotation of the star in the 1%-depth surface layers. The knowledge of this differential rotation, close to the surface, will help the modelling of a dynamo, which may be at the origin of the X-ray activity of Altair (Robrade & Schmitt 2009).

5.2. Discussion

The mode shown in Fig. 7 has been selected because of its (presumably) high visibility but we still ignore whether it is stable or not. Indeed, the foregoing computation neglected any non-adiabatic effect since preliminary non-adiabatic calculations showed inconclusive results for many reasons that we shall discuss now.

Indeed, gravito-inertial modes form a dense spectrum in the adiabatic limit. Namely, any frequency below $2f_{\text{rot}}$ is as close as we wish to a mode frequency (e.g. Dintrans et al. 1999). Moreover, the modes contain singularities, which appear as shear layers in the eigenfunctions (e.g. Dintrans et al. 1999; Rieutord et al. 2001; Rieutord & Valdetaro 2018). This makes the computation of gravito-inertial modes in a stellar model quite difficult. In particular, our attempts could not reliably compute the growth or the damping rates of the eigenmodes with frequencies in the range of the observed ones (e.g. Table 2).

If we leave aside the stability question, the density of frequencies in the spectrum is another difficulty. The observed frequencies listed in Tab. 2 have a limited precision of 0.05 c/d due to the short length of the time series. Our calculations show that in a frequency box of size 0.1 c/d a dozen of eigenmodes may be found if we only consider the least damped modes. Obviously, long time series will be needed to reduce this uncertainty.

On the theoretical side, the instability that drives the modes may not be of the usual nature, namely an exponential growth that is limited by a nonlinear coupling with

stable modes. Here, the spectral density of modes reveals the non-normality of the differential operator which governs the free oscillations. It allows the possibility of algebraic growth of perturbations (Schmid 2007; Rieutord 2015). In such a case the observed waves are not eigenmodes, but combinations of several eigenmodes.

The foregoing remarks underline the point that deciphering the waves frequencies at the surface of Altair will be a challenging task to which we reserve a dedicated work.

On the observational side, it is clear that long time series are needed to narrow the error box on frequencies and thus be of great help to identify the possible modes or quasi-modes that are observed.

6. Conclusions

In this paper we presented the first detection by spectroscopy of waves at the surface of Altair, a rapidly rotating star with an equatorial velocity likely over 300 km/s. We showed that the observed waves are in or near the frequency band $[-2f_{\text{rot}}, 2f_{\text{rot}}]$ in the frame co-rotating with the star. They are thus identified as inertial or gravito-inertial waves. The difference between inertial waves and gravito-inertial ones comes from the influence of the stable stratification of the fluid. Pure inertial waves are restored only by the Coriolis force and, in stars, appear in their convection zone (e.g. the recent detection of these waves in the Sun by Gizon et al. 2021), while gravito-inertial waves are restored both by buoyancy and Coriolis force. In Altair, thin convective layers exist close to the surface and may be the seat of pure inertial waves, which may drive a signature at the surface. An identification of observed waves with gravito-inertial waves is however more likely since convective layers are thin and separated by a radiative one. Finally, we note that the observed waves are characterized by rather high azimuthal wavenumbers, and propagate in the prograde direction. Their amplitude, in intensity, is of the order of 10^{-3} .

Altair was known as the "brightest δ Scuti" (Buzasi et al. 2005). We now see that its oscillation spectrum not only includes acoustic modes but also gravito-inertial waves. Low-frequency oscillations were actually already detected by Buzasi et al. (2005) and Le Dizès et al. (2021) in photometric data, but without constraints on the wavenumbers it was difficult to assign them a definite category (gravito-inertial, pure inertial or even acoustic) because of the high rotation frequency ($\sim 3c/d$) and a possible non-axisymmetric nature. Hence, Altair now appears as a hybrid oscillator but its fast rotation makes it still different from stars that show the hybrid state of δ Scuti and γ Doradus stars.

Our failure to identify more precisely the observed frequencies, using the best model of Altair (Bouchaud et al. 2020), shows that such an identification is difficult due to the spectral density of modes in or near the inertial frequency range. A dedicated work is therefore required to further progress in the interpretation of the observed frequencies, all the more that gravito-inertial modes are controlled by a non-normal differential operator in the adiabatic limit. This implies that the growth of the mode may be algebraic like in shear instabilities, and may excite a wide or ever changing oscillation spectrum (Schmid 2007).

On the observational side, further progress claims for longer time series to either give a more precise value to the frequencies, and to eventually monitor the presently detected oscillations. Moreover, it will be very interesting

to observe spectroscopically other fast rotators similar to Altair to see if such waves are also excited in stars with different fundamental parameters. α Ophiuchi (Ras Alhague) and α Cephei (Alderamin) are very good targets for such investigations because of their brightness, but the recent work of Ma et al. (2022) shows that Altair may have numerous sisters.

Acknowledgements. MR would like to thank S. Charpinet for enlightening discussions on the analysis of the time series. He also acknowledges the support of the French Agence Nationale de la Recherche (ANR), under grant ESRR (ANR-16-CE31-0007-01). GMM acknowledges support by “Contribution of the UGR to the PLATO2.0 space mission. Phases C / D-1”, 1032 funded by MCNI/AEI/PID2019-107061GB-C64. Computations of Altair’s models and eigenfrequencies have been possible thanks to HPC resources from CALMIP supercomputing center (Grant 2022-P0107).

References

- Baglin, A., Breger, M., Chevalier, C., et al. 1973, *A&A*, 23, 221
- Balona, L. A., Daszyńska-Daszkiewicz, J., & Pamyatnykh, A. A. 2015, *MNRAS*, 452, 3073
- Böhm, T., Zima, W., Catala, C., et al. 2009, *A&A*, 497, 183
- Bouchaud, K., Domiciano de Souza, A., Rieutord, M., Reese, D. R., & Kervella, P. 2020, *A&A*, 633, A78
- Buzasi, D. L., Bruntt, H., Bedding, T. R., et al. 2005, *ApJ*, 619, 1072
- Dintrans, B. & Rieutord, M. 2000, *A&A*, 354, 86
- Dintrans, B., Rieutord, M., & Valdetaro, L. 1999, *J. Fluid Mech.*, 398, 271
- Domiciano de Souza, A., Kervella, P., Jankov, S., et al. 2005, *A&A*, 442, 567
- Donati, J. F., Semel, M., Carter, B. D., Rees, D. E., & Collier Cameron, A. 1997, *MNRAS*, 291, 658
- Espinosa Lara, F. & Rieutord, M. 2013, *A&A*, 552, A35
- Gizon, L., Birch, A. C., & Spruit, H. C. 2010, *Ann. Rev. Astron. Astrophys.*, 48, 289
- Gizon, L., Cameron, R. H., Bekki, Y., et al. 2021, *A&A*, 652, L6
- Gonzalez Hernandez, I., Patron, J., Chou, D.-Y., & TON Team. 1998, *ApJ*, 501, 408
- Kochukhov, O., Makaganiuk, V., & Piskunov, N. 2010, *A&A*, 524, A5
- Kupka, F., Piskunov, N., Ryabchikova, T. A., Stempels, H. C., & Weiss, W. W. 1999, *A & A Suppl. Ser.*, 138, 119
- Le Dizès, C., Rieutord, M., & Charpinet, S. 2021, *A&A*, 653, A26
- López Ariste, A., Georgiev, S., Mathias, P., et al. 2022, *A&A*, 661, A91
- Ma, S., Esamdin, A., García Hernández, A., et al. 2022, to appear in *ApJ*, 1
- Monnier, J. D., Zhao, M., Pedretti, E., et al. 2007, *Science*, 317, 342
- Peterson, D., Hummel, C., Pauls, T., et al. 2006, *ApJ*, 636, 1087
- Reese, D. R., Mirouh, G. M., Espinosa Lara, F., Rieutord, M., & Putigny, B. 2021, *A&A*, 645, A46
- Reiners, A. & Royer, F. 2004, *A&A*, 428, 199
- Rieutord, M. 2015, *Fluid Dynamics: An Introduction* (Springer), 508 pp.
- Rieutord, M., Espinosa Lara, F., & Putigny, B. 2016, *J. Comp. Phys.*, 318, 277
- Rieutord, M., Georgeot, B., & Valdetaro, L. 2001, *J. Fluid Mech.*, 435, 103
- Rieutord, M. & Valdetaro, L. 1997, *J. Fluid Mech.*, 341, 77
- Rieutord, M. & Valdetaro, L. 2018, *J. Fluid Mech.*, 844, 597
- Robrade, J. & Schmitt, J. H. M. M. 2009, *A&A*, 497, 511
- Schmid, P. J. 2007, *Ann. Rev. Fluid Mech.*, 39, 129
- Spalding, E., Morzinski, K. M., Hinz, P., et al. 2022, *Astron. J.*, 163, 62
- Suárez, J. C., Bruntt, H., & Buzasi, D. 2005, *A&A*, 438, 633
- Takeda, Y. 2020, arXiv e-prints, arXiv:2012.15152
- van Belle, G. T., Ciardi, D. R., Thompson, R. R., Akeson, R. L., & Lada, E. A. 2001, *ApJ*, 559, 1155
- Ventura, R., Catanzaro, G., Christensen-Dalsgaard, J., di Mauro, M. P., & Paternò, L. 2007, *MNRAS*, 381, 1647
- Walker, G., Matthews, J., Kuschnig, R., et al. 2003, *Pub. Astron. Soc. Pacific*, 115, 1023